Lab on a Chip

PAPER

View Article Online
View Journal



Cite this: DOI: 10.1039/d3lc00073g

# Droplet-based microfluidic platform for viscosity measurement over extended concentration range†

Paul Cochard-Marchewka, * Nicolas Bremond and Jean Baudry

Received 25th January 2023,
Accepted 3rd April 2023

DOI: 10.1039/d3lc00073g

rsc.li/loc

Rheology of concentrated protein solutions is crucial for the understanding of macromolecular crowding dynamics as well as the formulation of protein therapeutics. The cost and scarcity of most protein samples prevents wide-scale rheological studies as conventional viscosity measurement methods require large sample volume. There is a growing need for a precise and robust viscosity measurement tool that minimizes consumption and simplifies the handling of highly concentrated protein solutions. This objective is achieved by combining microfluidics and microrheology: we developed a specific microsystem to study the viscosity of aqueous solutions at high concentrations. The PDMS chip allows *in situ* production, storing and monitoring of water-in-oil nanoliter droplets. We perform precise viscosity measurements inside individual droplets by particle-tracking microrheology of fluorescent probes. Pervaporation of water through a PDMS membrane induces aqueous droplet shrinking, concentrating the sample up to 150 times, thus allowing viscosity measurements along an extended concentration range in just one experiment. The methodology is precisely validated by studying the viscosity of sucrose solutions. Two model proteins are also studied with sample consumption reduced to as little as 1 μL of diluted solution, showcasing the viability of our approach for the study of biopharmaceuticals.

## 1 Introduction

*In vitro* studies often focus on the interaction of selected macromolecules in dilute systems, far from the reality of a highly concentrated and heterogeneous *in vivo* environment.[1] Most cells contain 20–30% of macromolecules in volume. Intracellular protein concentration is in the range 200–300 g $L^{-1}$, regardless of the type of cell, adding to an environment already packed with RNA (75–150 g $L^{-1}$).[2]

High-concentration experiments are necessary to better understand intracellular physics,[3] to characterize protein behavior in intra or extracellular mediums[4,5] or study enzymatic reactions[6,7] for example. In the case of biopharmaceutics, most notably monoclonal antibodies (mAbs), high-concentration viscosity characterization a crucial step in the formulation process,[8] as well as an important research field.[9] Biopharmaceutics sometimes need to be formulated at concentrations above 100 mg $mL^{-1}$. At such high concentrations, mAb–mAb interactions can cause a rapid, sequence-dependent[10] increase in viscosity.[11] For these formulation problems, and because viscosity represents a macroscopic measurement of protein–protein interactions,[12] the rheology of protein solutions is an important experimental field, often limited by the high sample volumes required by standard characterization experiments.[13]

By allowing the handling and analysis of fluid samples at the microscopic scale, microfluidics[14] represent a great stride in the search for a low sample consumption, with uses in analytical chemistry and biology.

In addition, droplet-based microfluidics, that relies on the production, manipulation and analysis of individual nanoliter compartments,[15] allows rapid screening of the parameters space, while limiting costly protein consumption.

The ability to precisely characterize reduced volumes is crucial for the rheological study of scarce samples such as proteins. As such, several in-chip viscosity measurement techniques have been recently developed.[16] Microrheology is an efficient way to measure viscosities inside microfluidic samples. Initially developed to measure viscosities within cells,[17] microrheology relies on the tracking of colloidal probes whose passive or active motion can be linked to the medium's properties.[18] It has since been successfully applied to microfluidic protein samples[13] as well as millifluidic droplets.[19]

In addition to manipulation and sorting of droplets, micro-devices have been designed to modify the concentration of the medium inside the droplets by dialysis. Removing water from the droplets, either through osmosis,

*Laboratoire Colloïdes et Matériaux Divisés, Institut Chimie, Biologie, Innovation, UMR 8231, ESPCI Paris, CNRS, Université Paris Sciences et Lettres, 75005 Paris, France. E-mail: paul.cochard-marchewka@espci.psl.eu*

† Electronic supplementary information (ESI) available. See DOI: https://doi.org/10.1039/d3lc00073g

pervaporation or dilution in the continuous phase, induces aqueous shrinking,[20] effectively concentrating the solutes. The reduced required sample size and the precise control over in-droplet concentration proves useful for analyte detection.[21] Protein crystallization is a costly and trial-and-error based process that is likewise greatly simplified by the use of micro-devices.[22,23]

We designed a device able to combine some of the aforementioned techniques, offering a simple and reliable platform for investigating viscous features of various hydrophilic compounds.

The accuracy and reliability of our approach were validated by studying samples of tabulated viscosity, pure water and sucrose solutions. The study of two model proteins showcased the efficiency of our method to characterize protein samples with minimal sample consumption. Our approach requires as low as 1 μL of dilute samples to perform full viscosity characterization of a given solute, as a step-emulsification geometry allows on-demand droplet production. Pervaporation-induced shrinking allows in-droplet concentration by a factor of 125 while viscosity is continuously measured by particle-tracking microrheology. Initially developed to explore a 1–200 mPa s viscosity range, corresponding to the viscosity range of biopharmaceutics, our method proved capable of accurate measurements on a 1 mPa s–5 Pa. range.

# 2 Material and methods

### 2.1 Microfluidic device

The 3-layer microfluidic device was obtained through soft lithography.[24] For each layer, a quartz/chromium photolithography mask was printed by direct laser exposure (μPG 101, Heidelberg Instruments). A multi-layer master was fabricated by exposing epoxy photoresist (SU-8, Kayaku Advanced Materials) with a mask aligner (MJB4, Süss MicroTec). The design of the 3 separate layers is visible in Fig. S1 of the ESI.†

### 2.2 Samples

Sucrose (179949), bovine serum albumine (A7906) and lysozyme from chicken egg white (L4919) were purchased from Merck KGaA. All samples were prepared with ultra-pure water (Milli-Q, Merck KGaA), and filtrated through 0.2 μm PTFE syringe filters (VWR).

### 2.3 Droplet production and manipulation

Novec 7500 (3 M, $\eta_{N7500} \approx 1.2$ mPa s) or Fomblin Y06/6 (Solvay, $\eta_{Y06} \approx 89$ mPa s) fluorinated oils were used as continuous phase, mixed with RAN-008 fluorosurfactant (RAN Biotechnologies) at a 0.2% w/w concentration. A 2-channel syringe pump (Nemesys, Cetoni GmbH) was used to inject both the continuous and dispersed phases. A peristaltic pump (Sci-Q 323, Watson Marlow) produced the air flow used for droplet shrinking.

### 2.4 Fluorescent probes

500 nm-diameter yellow-green fluorescent probes (FluoSpheres™, ThermoFisher Scientific, F8813) were encapsulated in the droplets at an initial solid volume fraction of $\phi_i = 4 \times 10^{-7}$, corresponding to ≈6 particles per nanoliter or ≈90 particles per droplet. The probes were tracked with an inverted microscope (Axio Observer 7, Zeiss) mounted with a 40× objective (EC Plan-Neofluar NA 0.75, Zeiss), a multicolor LED light source (Zeiss Colibri 7) and a CMOS camera (ORCA-Flash4.0 LT C11440, Hamamatsu Photonics). The probes were imaged in the droplet's equatorial plane, localized by autofocusing on the droplet's edge. For each acquisition, a continuous 1000-images fluorescence timelapse was performed with an exposure time $\tau = 100$ ms. The camera was used in streaming mode, with a delay between two images equal to the exposure time ($\Delta t = \tau = 100$ ms). One batch of tracers was grafted with-PEG chains (amine-PEG, $M_w = 20$ kDa, Rapp Polymer) following Garting & Stradner's protocol.[25] The type of tracers used will be specified in the subsequent results. The hydrodynamic radius of the probes was determined through dynamic light scattering (ZetaSizer Ultra, Malvern Panalytical).

### 2.5 Particle detection & tracking

Post-acquisition data analysis, mainly particle detection & tracking, diffusion coefficient estimation and droplet volume measurement, was performed with a custom-made MATLAB script. The .czi files and their metadatas were read with the Bio-Formats toolbox[26] (Open Microscopy). The particles' positions were detected on each of the 1000 frames of the time-lapse. After thresholding to reduce background noise, a first peak detection was performed to roughly localize the brightest spots of the image. Then, a centroid fit was used to localize the center of the tracers with sub-pixel accuracy[27] (10 nm typical accuracy for fixed particles).

A Crocker–Grier algorithm[28] was then used to build particular trajectories. For each of the detected trajectory, a $(\Delta x_n, \Delta y_n)_{n \in [1,N_i]}$ matrix of particular displacement was obtained, with $N_i$ the length of the $i$ trajectory. We only considered continuous trajectory longer than 100 frames. An average of 30 trajectories were detected per acquisition, with a typical length of 300 frames. A covariance-based estimator (CVE) was used to estimate diffusion coefficients from trajectory data. Recently developed by Christian L. Vestergaard,[29] this regression-free estimator provides unparalleled accuracy compared with the standard MSD or MLE-based estimators, given our experimental parameters. From the displacement matrix, the diffusion coefficient for a given trajectory is estimated as:

$$\hat{D}_i = \frac{\left\langle (\Delta x_n)^2 \right\rangle + \left\langle (\Delta y_n)^2 \right\rangle}{4\Delta t} + \frac{\langle \Delta x_n \Delta x_{n+1} \rangle + \langle \Delta y_n \Delta y_{n+1} \rangle}{2\Delta t} \quad (1)$$

The Stokes–Einstein law was then used to estimate the dynamic viscosity associated with each trajectory:

 

$$\hat{\eta_i} = \frac{k_B T}{6\pi r \hat{D}_i} \quad (2)$$

with $k_B$ the Boltzmann constant, $T$ the temperature and $r$ the probe radius. The estimated global measured viscosity $\hat{\eta}$ was obtained as the average of the estimates provided for each trajectory, weighted by the trajectory length:

$$\hat{\eta} = \frac{\sum_{i=1}^{T} N_i \hat{\eta_i}}{\sum_{i=1}^{T} N_i} \quad (3)$$

Correlation assessment between the measured viscosity and various experimental parameters was performed by calculation of the Spearman's rank correlation coefficient $\rho$ on statistically significant data sets. Spearman's correlation measures rank correlation, with extreme values of $\rho = \pm 1$ indicating the variables are perfectly monotone functions of each other. The $p$-value indicates the statistical significance of any correlation between the variables. We adopted the common convention that the correlation is only statistically significant for $p$-values lower than 0.05.[30]

### 2.6 Droplet volume measurement

In-chip concentration monitoring was performed through droplet volume measurement.

Edge detection of the spherical droplets was performed by circular Hough transform[31] on brightfield images. The detected droplet radius gave access to their volume, and in turn to the solute's in-droplet concentration as the sample's initial concentration was known.

We estimate the error on droplet volume measurement to be $<5\%$ in the vast majority of the cases. This estimation is detailed in the supplementary information. In particular, edge detection was validated with optical models.[32]

### 2.7 Concentration

Samples of known initial mass concentration $c_0$ were prepared. This concentration is defined as:

$$c_0 = \frac{m_s}{V_T} \quad (4)$$

With $m_s$ the mass of solute and $V_T$ the solution's total volume.

At any given time, volume measurement gave access to the in-droplet mass concentration:

$$c(t) = c_0 r(t) \quad (5)$$

With $r(t) = \frac{V_0}{V(t)}$ the droplet's shrinking ratio.

For sucrose samples, the results were expressed in terms of mass fraction. The mass fraction of a solution is defined as:

$$c_{w/w} = \frac{m_s}{m_T} \quad (6)$$

With $m_T$ the total mass of the solution.

To perform the conversion between $c$ and $c_{w/w}$, the partial specific volume of sucrose[33,34] ($\bar{v}$ = 0.62 mL g$^{-1}$) was taken into account. The mass fraction inside the droplet was expressed as:

$$c_{w/w}(t) = \frac{r(t) m_s}{m_w + [\bar{v} + (1-\bar{v}) r(t)] m_s} \quad (7)$$

With $m_s$ and $m_w$ the masses of solute and water in the initial solution.

Protein samples of known initial mass concentration $c_0$ were studied. The results were expressed in terms of effective volume fraction, defined as:[35]

$$\phi_{eff} = k_0 \times c \quad (8)$$

with $c$ the mass concentration and $k_0$ the voluminosity of the proteins, defined as:

$$k_0 = \frac{4}{3}\pi \frac{N_A}{M_w} {R_S}^3 \quad (9)$$

with $N_A$ the Avogadro constant, $M_w$ the protein's molar mass and $R_S$ their Stokes radius. The values of $R_S^{bsa}$ = 3.5 nm and $R_S^{lys}$ = 2 nm were considered for BSA[36] and lysozyme[37] respectively.

## 3 Results and discussion

### 3.1 Results

**3.1.1 Device operation.** Fig. 1 shows schematic view of the whole chip, as well as a detailed view of its rheological section.

The first section of the chip is a dropmaker. The use of a step-emulsification geometry allows on-demand production of droplets[38,39] by bursts of 10–20 droplets corresponding to 150–300 nL of sample. This geometry, combined with a syringe pump-based injection technique, allowed us to perform successful experiments using as little as 1 μL of diluted solution. A detailed view of the dropmaker and its dimensions is visible in Fig. S2 of the ESI.† A movie showing the production of a droplet burst is visible in the ESI.†

Once produced, droplets are stored in a selection chamber, just upstream of the main channel. Precise flow control allows to individually select and load droplets in cylindrical wells located above the main channel. The wells have a 300 μm diameter and a 300 μm depth. Flow control is achieved by precise tuning of the differential height between the inlet and the outlet, see Fig. S3 of the ESI.† The loading is gravitational, as the water droplets are lighter than the fluorinated continuous phase ($\Delta\rho$ = 614 kg m$^{-3}$ in the case of Novec 7500). By shielding the droplets from residual flow in the main channel, the wells allow stabilization of the droplets, essential for MPT microrheology. Once loading is complete, droplet shrinking is achieved by water

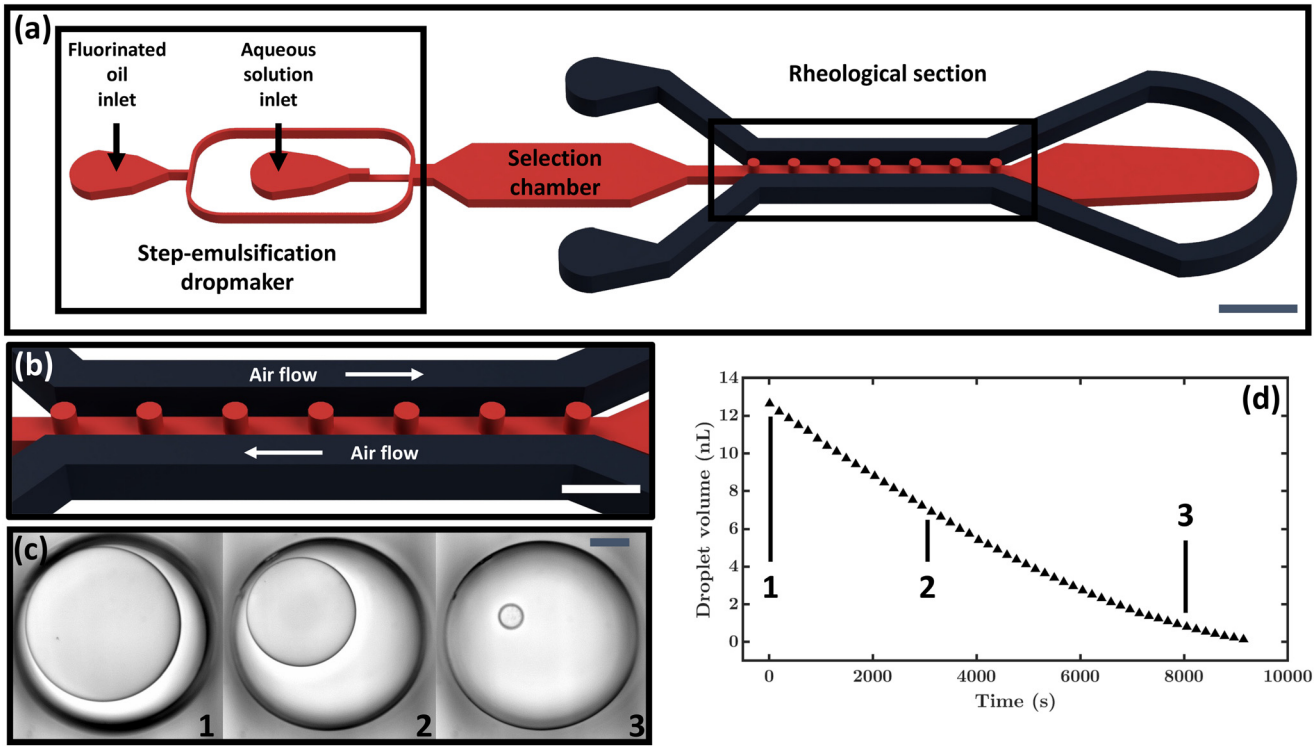


**Fig. 1** Overview of the microfluidic device's architecture and of the droplet shrinking process. (a) Schematic, perspective view of the microfluidic device. The step-emulsification geometry allows on-demand production of droplets following injection of the continuous phase (fluorinated oil) and dispersed phase (aqueous solution). After production, droplets are briefly stored in a selection chamber before being individually selected and loaded into the rheological section (scale bar: 2000 μm). (b) Schematic, perspective view of the rheological section. Between the selection chambers, the main channel narrows to reach a width of 400 μm. Above the main channel, 7 cylindrical wells of 300 μm diameter serve as traps, as the lighter water droplets tend to rise in the wells. Separated by a 200 μm PDMS membrane, the lateral channel surrounds the rheological section. Air flow through the lateral channel maintains a humidity gradient between the dry air and the water droplets, inducing water pervaporation through the PDMS membrane and thus droplet shrinking (scale bar: 1000 μm). (c) Brightfield microscopy images of a water droplet at different shrinking stages (40×, scale bar: 50 μm). (d) Measured droplet volume as a function of time. Continuous droplet shrinking is monitored *via* edge detection of the spherical droplet. The points corresponding to the 3 images shown in (c) are indicated.

pervaporation through the 200 μm PDMS membrane between the main and lateral channels.[22,23] Air flow in the lateral channel keeps the humidity gradient constant and is imposed by a peristaltic pump.

Experimentally, the shrinking speed as a function of membrane thickness behaves as described by previously established pervaporation models.[20] Depending on the solute, the shrinking speed can then be adjusted by changing either the membrane's width or the humidity of the air flow. In our case, a 200 μm-wide membrane minimizes the experiment time while ensuring homogeneity of the droplet's content.[40]

**3.1.2 Validation of particle-tracking microrheology.** To assess the accuracy of our particle-tracking microrheology method, we first measured the viscosity of pure water without any droplet shrinking. On 3 droplets of distinct radius, a series of 20 successive time-lapses was performed. The results, reported in Table 1, showcase the accuracy and the repeatability of our measurements, with an average relative standard-deviation (RSD) of around 3%. Additionally, these experiments allowed us to evaluate the correlation between measured viscosity and particular position. Fig. 2 displays the heatmap of viscosities measured in the equatorial plane of a pure water droplet. Each point corresponds to the mean particle position for a given detected trajectory. The variations in measured viscosity do not correlate with the particles position in the equatorial plane. To study the influence of the shrinking process we monitored the viscosity of shrinking water droplets, whose viscosity remains constant regardless of shrink. Fig. 3 shows the combined results of 4 distinct shrinking experiments. These experiments tend to

**Table 1** Measured viscosities in pure water droplets, without shrinking. On each of the 3 droplets, a series of 20 successive time-lapses were recorded. The measured viscosities $\hat{\eta}$ are to be compared with the tabulated value of 0.89 mPa s for water at 25 °C

| Experiment | 1 | 2 | 3 |
|---|---|---|---|
| Droplet radius (μm) | 95 | 140 | 62 |
| Mean viscosity $\langle\hat{\eta}\rangle$ (mPa s) | 0.88 | 0.85 | 0.87 |
| Relative error $\left\langle \frac{\lvert\hat{\eta}-\eta\rvert}{\eta} \right\rangle$ | 1% | 4.5% | 2% |
| RSD $\frac{\sigma(\hat{\eta})}{\langle\hat{\eta}\rangle}$ | 2.8% | 2.9% | 3.4% |

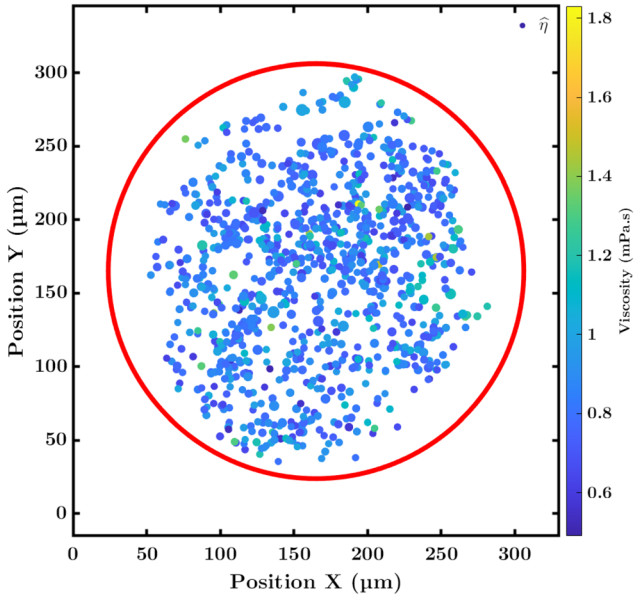


**Fig. 2** Measured viscosity heatmap on the equatorial plane of a pure water droplet. The position of each point corresponds to the mean particular position for each of the 996 trajectories tracked. The point's color codes for the measured viscosity, and its size codes for the trajectory length. The red circles corresponds to the position of the droplet's edge. These data have been obtained on a total of 20 acquisitions performed on a 140 μm radius water droplet (droplet 2 in Table 1).

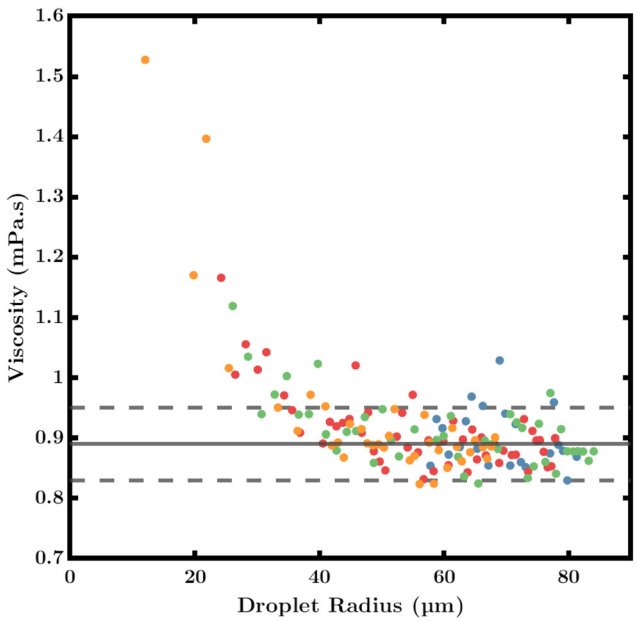


**Fig. 3** Measured viscosities for shrinking pure water droplets. Combined data from 4 distinct shrinking experiments, corresponding to a total of 197 acquisitions. Each points corresponds to one acquisition, with colors coding for the 4 different shrinking droplets. For lower droplet radii ($R < 30$ μm), an increase of measured viscosity $\hat{\eta}$ seem to indicate an influence of the droplet's interface on particular diffusion. The two dashed lines represent the confidence interval for MPT estimated from the acquisitions on fixed-radius droplets (Table 1).

indicate that the shrinking process has no significant effect on particular diffusion until lower droplet radii under 30 μm.

**3.1.3 Characterization of the accessible range.** To demonstrate the range of our experimental approach, we then measured the viscosity of sucrose solutions. Sucrose presents a good solubility in water, allowing the study of a wide concentration range. Over this range, its viscosity continuously increases, covering 4 decades (1 mPa s–10 Pa s), making sucrose a compound of choice to assess both the concentration and viscosity ranges accessible to our approach. Sucrose viscosity has been tabulated with high precision,[41] and as such it has been previously used as a calibration agent for microrheology.[13]

Starting from dilute solutions (5% w/w), droplet shrinking allowed us to reach concentrations as high as 80% w/w. Fig. 4 shows a good comparison between the experimental relative viscosity profile of sucrose and the tabulated values. Relative viscosity is defined as:

$$\eta_{\mathrm{rel}} = \frac{\eta}{\eta_0} \tag{10}$$

with $\eta_0$ the dynamic viscosity of the solvent, in our case water.

20 experiments were conducted, with varying initial concentrations and droplet radii. To estimate the precision of these experiments, we performed a linear interpolation between our data and the tabulated values before measuring the distance between the two curves. On the target 1–200

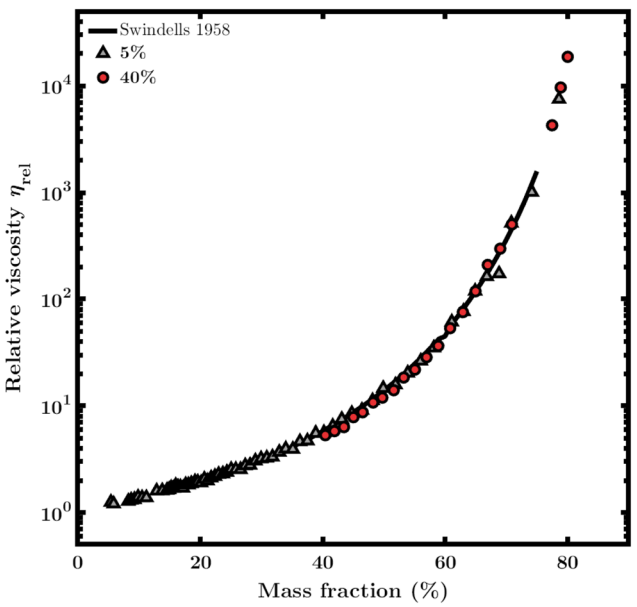


**Fig. 4** Relative viscosity as a function of mass fraction for aqueous sucrose solutions, comparing microrheology in shrinking droplet results (△) and tabulated data[41] (solid line). Two distinct experiments are reproduced here, with initial sucrose mass fraction of 5% and 40% respectively. For clarity, only 1 out of 5 data points have been reproduced. A similar fig. with all measured data points is available in ESI.†

mPa s range, the average relative error was around 3%. The measured viscosities compare well with the tabulated until around 1.7 Pa s corresponding to 75% w/w. Above this value, in the 75–80% range, viscosities as high as 18 Pa s were measured. While these values have no tabulated value to compare with, they qualitatively match the general trend of sucrose's viscosity curve.

For viscosities above 200 mPa s, a more viscous fluorinated oil was used as the continuous phase to prevent noise caused by droplet movement (see 3.2.3).

**3.1.4 Proteins.** Finally, we applied our approach to the study of two model proteins dissolved in pure water: bovine serum albumin and lysozyme. For these experiments, the fluorescent probes were grafted with-PEG polymer chains, allowing the particles to remain stable regardless of the studied protein's charge. With this steric stabilization,[25] the same probes can be used to work with either negatively charged proteins, such as BSA, or positively charged ones, such as lysozyme. With the use of a syringe pump-based injection system, we were able to conduct these experiments using as little as 1 μL of diluted initial solutions, demonstrating our approach's contribution to the reduction of sample consumption. For these two model proteins, all concentrations give a viscosity within our approach's measuring range. Fig. 5 shows the relative viscosity (*cf.* eqn (10)) profile for the two proteins.

### 3.2 Discussion

**3.2.1 Influence of droplet interface.** One of the novelties of our approach is the use of MPT microrheology in microfluidic droplets. The Stokes–Einstein law (eqn (2)) relies on the hypothesis of free diffusion. In reality, the liquid–liquid interface at the edge of the droplet will affect the diffusion of the probes.[42] The rigidity of the surfactant-covered interface[43,44] will induce an increase of the particle's drag at its vicinity, that will in turn results in a decrease of the particle's diffusion coefficient and an increase of viscosity measured through the Stokes–Einstein equation. The influence of the interface is anisotropic, whether the particle is experiencing diffusion normal or parallel to the interface.[45] Previous instances of in-droplet microrheology have been performed in millifluidic-sized droplets,[19] where particle tracking could be performed at a distance where any influence from the interface was negligible. For bigger droplets, the interface can be approximated as plane, and the diffusion coefficient decrease can be calculated.[46] For example, a particle experiencing normal diffusion at 5 μm of the interface will display a 5% diffusion coefficient decrease. At 100 μm, the diffusion coefficient decrease drops to just 0.3%.

The important number of acquisitions performed on pure water droplets without shrinking (see Fig. 2) provided us with a data set statistically significant enough to perform correlation assessment. With a correlation coefficient of $\rho$ = 0.017, and a $p$-value of 0.59 no correlation was found between the particle's position relative to the center of the droplet. For these droplets (Fig. 2 was obtained with a 140 μm-radius droplet), the interface seems to have no influence on particular diffusion. This results can be interpreted as such: not only the area where the effects of the interface are sizable is a small fraction of the area of the equatorial plane for bigger droplets but in addition the probes will diffuse in and out of this area during the acquisition, as the characteristic diffusion length is $l_c = \sqrt{D\Delta t} \approx 7$ μm for probes diffusing in water during a 30 s time frame, corresponding to the average trajectory length.

This result might not hold for smaller droplets, as the area in the vicinity of the interface will increase in size relative to the equatorial plane, and as the increased confinement will prevent the probes from diffusing in and out of this area. Our goal of individual droplet manipulation, and our aim to continuously concentrate samples by droplet shrinking mandates us to work with droplets of reduced radius ($R < 50$ μm), a range previously unexplored. Additionally, at smaller radii the droplet's interface can no longer be considered as a plane. We monitored the viscosity of shrinking water droplets (see Fig. 3). For droplets under 30 μm in radius there is an increase in measured viscosity, potentially due to restrained diffusion caused by the droplet's interface.

We could only perform those experiments at the lowest bound of our viscosity range, the viscosity of pure water. Indeed water is the only compound whose viscosity is constant regardless of droplet shrinking. However, we studied the viscosity of sucrose solutions with various initial concentrations and initial droplet radii. The repeatability and continuity of the measured viscosities for more than 20 experiments tend to indicate that given our experimental conditions, the droplet's interface has no effect on the measured viscosity.

**3.2.2 In-droplet homogeneity.** By averaging the measured viscosity over all the detected trajectories, multi-particle tracking relies on the assumption that the viscosity is constant across the droplet's equatorial plan. Inhomogeneity

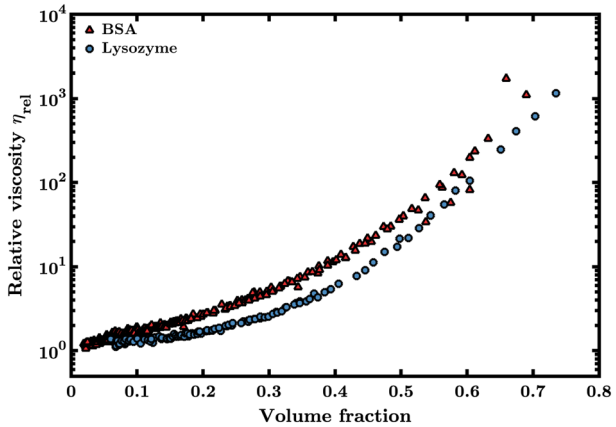


Fig. 5 Relative viscosities for bovine serum albumin (BSA) △ and lysozyme (○) in pure water.

 

of the solutes inside the droplet could jeopardize this assumption. Depending on the shrink speed and on the solute's diffusion coefficient, an accumulation of solute could occur at the droplet's interface. As developed in previous studies,[40] a colloidal suspension in a shrinking droplet can be considered homogeneous at Pe $\ll$ 1, with Pe the Péclet number defined as:

$$\mathrm{Pe} = \frac{Rv}{D} \tag{11}$$

$R$ is the droplet radius, $v$ is the speed of the interface shrinking towards the center of the droplet, and $D$ is the solute's diffusion coefficient. This condition is met for our experiments, with a maximum value at $\mathrm{Pe}^{\max} \approx 0.06$. Moreover, individual particle tracking in the equatorial plane revealed no evidence of any recirculation flow that could have indicated diffusion cause by solute gradient. Finally, it is important to remind that the shrinking speed can be tuned by changing our setup's PDMS membrane width. Should any solute inhomogeneity appear, one could easily tune the shrinking speed to reduce Pe.

**3.2.3 Influence of droplet movement.** As the spherical droplet is not confined by the cylindrical well, it will experience Brownian diffusion itself. We defined the ratio $\kappa$, comparing the characteristic Brownian diffusion lengths of the fluorescent probes and of the droplet itself:

$$\kappa = \frac{\sqrt{2D\Delta t}}{\sqrt{2D_\mathrm{d}\Delta t}} = \frac{\sqrt{D}}{\sqrt{D_\mathrm{d}}} \tag{12}$$

with $D_\mathrm{d}$ the diffusion coefficient of the droplet. Both $D$ and $D_\mathrm{d}$ can be expressed by the Stokes–Einstein law (eqn (2)) and (12) simplifies as:

$$\kappa = \sqrt{\frac{\eta_\mathrm{c}}{\eta}\frac{R}{r}} \tag{13}$$

with $R$ the droplet's radius, $r$ the probe's radius and $\eta_\mathrm{c}$ the viscosity of the continuous phase. As the droplet shrinks its radius will decrease and, with the exception of pure water, in-droplet viscosity will increase as the sample is concentrated. Decreasing droplet radius will induce an increase of droplet movement, and increasing in-droplet viscosity will decrease probe movement. For low values of $R$ and high values of $\eta$, droplet movement will be in the same order of magnitude as probe movement, lowering the precision of MPT microrheology. Two factors will then define the upper viscosity limit measurable by our approach: the precision of particle-tracking and droplet movement. A rough estimate of the maximum measurable viscosity can be calculated by placing the limit at $\kappa$ = 1. The maximum viscosity $\eta_\mathrm{d}^{\max}$ can then be defined as:

$$\eta_\mathrm{d}^{\max} = \eta_\mathrm{c}\frac{R}{r} \tag{14}$$

It is important to note that this value is likely to be underestimated, as the diffusion of the droplet is hindered its contact with the top of the well. Some sucrose experiments were conducted with Novec 7500 as a continuous phase, a fluorinated oil with relatively low viscosity. At high viscosities ($\eta >$ 300 mPa s) and low radii ($R <$ 30 μm), some experiments displayed a plateau, seemingly indicating that the maximum measurable viscosity had been reached (data from these experiments is visible in the ESI†). Moreover, the plateau was in the vicinity of the estimate provided by eqn (14). Derived from eqn (14), two solutions allow to push this limit and extend the viscosity range. The first is to increase the droplet radius $R$, thus limiting its movement. However, the drawback of this approach is the limitation of the maximum shrink factor. The second approach, which we have retained, is to increase $\eta_\mathrm{c}$, the viscosity of the continuous phase. By using Fomblin Y06 ($\eta_{\mathrm{Y06}}$ = 89 mPa s), eqn (14) estimates a limit of 4.8 Pa s for $R$ = 20 μm, much higher than the 0.1 Pa s estimated for Novec 7500 ($\eta_{\mathrm{N7500}}$ = 1.2 mPa s). Using a more viscous continuous phase did not present any additional difficulties in the operation of the device. With Fomblin Y06, no plateau behavior was observed, even for viscosities above 5 Pa s (see Fig. 4). Working with a more viscous continuous phase is an easy experimental approach to solving the issue of droplet movement.

It is also worth mentioning that particle-tracking on a fluctuating substrate is a well-studied problem, and that other more complex approaches such as two-point microrheology[47,48] are also available to cancel the noise caused by droplet movement.

**3.2.4 Precision of particle tracking microrheology.** To assess the precision of our MPT method, we took two values into account: the average relative error $\left\langle \frac{|\hat{\eta}-\eta|}{\eta} \right\rangle$ and the relative standard-deviation (RSD) $\frac{\sigma(\hat{\eta})}{\langle\hat{\eta}\rangle}$. The first value reflects any bias of our estimation, while the second quantifies its precision. For water, a slight bias was observed, as the viscosity was consistently underestimated. Such a bias can be linked with an error on the probes hydrodynamic radius, or on the measured temperature, both leading to a systematic error on the measured viscosity (see eqn (2)). To limit the influence of this bias, the measured viscosities are expressed in terms of relative viscosity $\eta_{\mathrm{rel}}$ (see eqn (10)).

For both water and sucrose, a 3% RSD on the viscosity was consistently observed. Several factors explain this value. First, the standard deviation of the CVE estimator can be quantified as:[29]

$$\sigma(\hat{D}) = \langle\hat{D}\rangle\sqrt{\frac{6+4\varepsilon+2\varepsilon^2}{N}+\frac{4(1+\varepsilon)^2}{N^2}} \tag{15}$$

where $\varepsilon = \frac{1}{\mathrm{SNR}^2} - \frac{1}{3}$ is linked to the signal-to-noise ratio of the particle tracking and $N$ is the number of detected positions. The signal-to-noise ratio is defined as $\mathrm{SNR} = \frac{\sqrt{D\Delta t}}{\sigma}$, the ratio between the characteristic length of

particular diffusion and the localization error. Both the experimental parameters of our optical acquisition method and our choice of particles were guided by the optimization of the SNR, with necessary compromises. For example, because our camera is in streaming mode, the shutter speed is equal to the interval between two consecutives images, $\tau = \Delta t$. Increasing the exposure time $\tau$ then results in an increased particular diffusion length, thus improving the SNR. However as the exposure time increases, motion blur will eventually cause the localization error $\sigma$ to increase as well. The same conflicting effects guides the choice of fluorescent probes. As the diffusion coefficient is inversely proportional to the probe's radius, the characteristic diffusion length can be increased by decreasing the probe's radius. However, as probe fluorescence is proportional to probe volume, decreasing their radius will also result in a increased localization error, affecting the SNR. For any microrheology experiment, each of these experimental parameters has to be optimized to find the best compromise for the SNR. In our case, droplet shrinking brings an additional layer of complexity. As particular diffusion is inversely proportional to viscosity, it is easy to see that optimal values of $\tau$ and $r$ will depend on the viscosity of the medium. Our choice of parameters ($\tau$ = 100 ms and $r$ = 250 nm) provides high SNR values on a wide range ($\eta \in$ [1 mPa s, 1 Pa s]). In the case of water, and more broadly for viscosities below 10 mPa s, eqn (15) can be simplified as:[29]

$$\frac{\sigma\left(\hat{D}\right)}{\left\langle \hat{D} \right\rangle} \approx \frac{\sqrt{5}}{\sqrt{N}} \tag{16}$$

For the experiments presented in Table 1, an average of $\langle N \rangle \approx$ 7800 positions were detected at each acquisition, giving an approximate RSD of ≈2.5%, an estimation in adequation with the experimental value of 3%.

Another source of error is the uncertainty on the radius of the fluorescent probes. Once the diffusion coefficient estimated, particle radius $r$ is involved in the calculation of the viscosity $\eta$ (see eqn (2)). A polydispersity of $\sigma_p \approx 14\%$ in diameter was measured by dynamic light scattering. The RSD caused by particle polydispersity can be estimated as:

$$\frac{\sigma\left(\hat{D}\right)}{\left\langle \hat{D} \right\rangle} = \frac{\sigma_p}{\sqrt{P}} \tag{17}$$

where $P$ is the number of distinct particles tracked during a given acquisition. With an average of $\langle P \rangle \approx 20$ distinct particles tracked, polydispersity-linked error is estimated as $\delta \approx 2.5\%$ for our experiments. These results show that in our experimental conditions two main factors limit the precision of MPT microrheology: the number of measured particular positions and the number of individual particles.

# 4 Conclusion

We developed an integrated platform, allowing viscosity characterization of aqueous solutes on an extended concentration range, starting from reduced volumes of dilute samples. Droplet shrinking, induced by water pervaporation through the microfluidic device, allows continuous concentration up to 150-fold of the solute throughout the experiment, while particle-tracking microrheology allows continuous viscosity measurement.

The use of the CVE estimator, along with a wide spectrum error sources quantification effort provides precise viscosity measurement on the 1–200 mPa s initial range of interest, as well as an extension of this range up to viscosities above 5 Pa s. Furthermore, the study of sucrose revealed our method's ability to easily reach extremely high concentrations, well above sucrose solubility in water of around 67%. The homogeneity brought by the small volume of the studied droplets and the absence of liquid–solid or liquid–gas interface greatly reduces nucleation, and the small volumes of the droplet increases the mean nucleation time[49] ($\propto 1/V$), allowing to probe supersaturated solutions without the crystallization-linked complications or the complexity of sample preparation encountered in macroscopic experiments.[50] However, the liquid–liquid interface of the droplets still presents a potential risk: protein adsorption/desorption at the water–oil interface during the shrinking process could affect the bulk protein concentration. Our experiments were performed with droplets of various initial volumes and with solutions of various initial concentrations. The fact that our results overlap into a continuous viscosity curve attests that in our case this potential effect does not noticeably impact bulk protein concentration, but it could become significant for studies with very low initial protein concentrations.

Because it relies on volume measurement to access concentration, our approach provides results based on mass concentration. This presents no obstacle for protein rheology, as results are by convention expressed in effective volume fraction. Some industrial application such as biopharmaceutics formulation might require conversion to mass fraction. As mentioned for the study of sucrose, the knowledge of the solute's partial specific volume is necessary to perform this conversion. This should not be an obstacle either, even for previously unstudied biopharmaceuticals, as the partial specific volume of proteins has been shown to be constant inside broad families.[51] For monoclonal antibodies specifically, representing the vast majority of biopharmaceutics, a constant value of $\bar{\nu}$ = 0.73 g mL$^{-1}$ is considered.[52]

The presence of excipients or buffer media might limit the concentration range accessible to our device. As droplet shrinking induces sample concentration, any buffer or additive will get concentrated by the same factor, potentially affecting the sample's viscous behavior. It remains possible to study these kind of samples by dividing the viscosity curve in 2 or 3 distinct segments, and by adjusting the initial excipient concentration to avoid any interference. Even if this approach diminishes the convenience of plotting the entire curve in a single experiment, our device remains a cost-effective and time-efficient method for the study of

 

biopharmaceuticals. Solvent conditions, most notably pH and ionic strength, can affect the viscous behavior of protein solutions. As such, the vast majority of available studies on the viscosity of proteins are performed in controlled solvent conditions. To fully validate the use of our approach for the study of protein solutions, additional experiments will be required with controlled solvent conditions and further purification. Without these additional steps, it is not yet possible to compare our data with previous work on the viscosity of BSA[53] and lysozyme.[54]

Showcasing the growing interest around this field, an device similar to ours was recently developed[55] with the aim of studying monoclonal antibodies in the future. Based on the same principle, this other work relies on a different microfluidic device, where the droplet are confined during the whole shrinking process. It is an advantage, as it eliminates the potential noise caused by droplet motion and thus does not require the use of more viscous continuous phase. By design, this other device relies on water pervaporation through the body of the microfluidic chip, whereas our device's lateral channel allow faster pervaporation and thus significantly shorten experiment times: from 24 h to 3 h, an 8-fold improvement. With such experiment times, we did not encounter any probe sedimentation issues and our device does not require the use of a rotator. Further reduction of the experiment time can be achieved by thinning the membrane between the main and lateral channel, as we found out the droplet's shrinking time was roughly proportional to the membrane's thickness. The device presented in this article has a 200 μm membrane, but we were able to produce devices with membrane thicknesses as low as 20 μm. However, one should keep in mind that increasing the droplet's shrinking speed might jeopardize in-droplet homogeneity, as previously discussed in 3.2.2.

Regardless of the device used, we highly recommend the use of Vestergaard's covariance-based estimator. It increases microrheology's precision, decreases the required number of particles and allows the quantification of the error made during particle tracking. Being regression-free, it is also significantly faster. The choice of this algorithm allowed us to expand our dynamic range 10-fold compared to the previous approach[55] and to measure viscosities 10 times higher. The precision of viscosity measurement and the maximum measurable viscosity could be increased by improving the imaging setup for particle tracking. By using a triggered camera, one could reduce the exposure time $\tau$ and increase the interval between two consecutive images $\Delta t$, which would decrease motion blur and increase diffusion lengths. Increasing the maximum viscosity might not be useful for protein rheology but can find applications in other fields, such as polymer rheology. Finally, we are able to work with smaller droplets, increasing the maximum shrinking factor (150 compared to 30 in the previous work) and allowing our device to work with smaller protein samples (10 μg for our approach compared to 1 mg in the previous work).

Understanding the behavior of concentrated protein solutions is crucial, as most biological media present high macromolecular concentrations, and as protein's collective behavior is linked with biological phenomena such as degenerative diseases.[56] By greatly simplifying the precise study of high-viscosity samples of highly concentrated proteins, our device could be an important tool in this effort.

## Conflicts of interest

There are no conflicts to declare.

## Acknowledgements

This research received funding from BPIFrance under the "Investissement d'Avenir" framework (CELLIGO project). This work also received the support of "Institut Pierre-Gilles de Gennes" (Laboratoire d'Excellence, "Investissements d'Avenir" program ANR-10-IDEX-0001-02 PSL, ANR-10-EQPX-34 and ANR-10-LABX-31). Special thanks to Kevin Phan at IPGG who has been of great help during prototyping.

## Notes and references

1 G. Rivas and A. P. Minton, *Trends Biochem. Sci.*, 2016, **41**, 970–981.
2 R. J. Ellis, *Curr. Opin. Struct. Biol.*, 2001, **6**, 114–119.
3 J. A. Dix and A. Verkman, *Annu. Rev. Biophys.*, 2008, **37**, 247–263.
4 A. Stradner, H. Sedgwick, F. Cardinaux, W. C. K. Poon, S. U. Egelhaaf and P. Schurtenberger, *Nature*, 2004, **432**, 492–495.
5 G. Foffi, G. Savin, S. Bucciarelli, N. Dorsaz, G. M. Thurston, A. Stradner and P. Schurtenberger, *Proc. Natl. Acad. Sci. U. S. A.*, 2014, **111**, 16748–16753.
6 G. B. Ralston, *J. Chem. Educ.*, 1990, **67**, 857.
7 A. Zotter, F. Bauerle, D. Dey, V. Kiss and G. Schreiber, *J. Biol. Chem.*, 2017, **292**, 15838–15848.
8 M. A. Woldeyes, W. Qi, V. I. Razinkov, E. M. Furst and C. J. Roberts, *J. Pharm. Sci.*, 2019, **108**, 142–154.
9 N. Skar-Gislinge, M. Ronti, T. Garting, C. Rischel, P. Schurtenberger, E. Zaccarelli and A. Stradner, *Mol. Pharmaceutics*, 2019, **16**, 2394–2404.
10 S. Yadav, A. Sreedhara, S. Kanai, J. Liu, S. Lien, H. Lowman, D. S. Kalonia and S. J. Shire, *Pharm. Res.*, 2011, **28**, 1750–1764.
11 J. Liu, M. D. Nguyen, J. D. Andya and S. J. Shire, *J. Pharm. Sci.*, 2005, **94**, 1928–1940.
12 Z. Zhang and Y. Liu, *Curr. Opin. Chem. Eng.*, 2017, **16**, 48–55.
13 L. L. Josephson, E. M. Furst and W. J. Galush, *J. Rheol.*, 2016, **60**, 531–540.
14 G. M. Whitesides, *Nature*, 2006, **442**, 368–373.
15 S.-Y. Teh, R. Lin, L.-H. Hung and A. P. Lee, *Lab Chip*, 2008, **8**, 198.
16 K. Shiba, G. Li, E. Virot, G. Yoshikawa and D. A. Weitz, *Lab Chip*, 2021, **21**, 2805–2811.
17 T. G. Mason, K. Ganesan, J. H. van Zanten, D. Wirtz and S. C. Kuo, *Phys. Rev. Lett.*, 1997, **79**, 3282–3285.

18 T. M. Squires and T. G. Mason, *Annu. Rev. Fluid Mech.*, 2010, **42**, 413–438.
19 K. M. Schultz and E. M. Furst, *Lab Chip*, 2011, **11**, 3802.
20 P. Bacchin, J. Leng and J.-B. Salmon, *Chem. Rev.*, 2022, **122**, 6938–6985.
21 M. R. G. Kopp, M. Linsenmeier, B. Hettich, S. Prantl, S. Stavrakis, J.-C. Leroux and P. Arosio, *Anal. Chem.*, 2020, **92**, 5803–5812.
22 J.-U. Shim, G. Cristobal, D. R. Link, T. Thorsen, Y. Jia, K. Piattelli and S. Fraden, *J. Am. Chem. Soc.*, 2007, **129**, 8825–8835.
23 S. Morais, G. Clisson, T. F. Mastropietro, M. L. Briuglia, J. H. ter Horst, J. Leng and J.-B. Salmon, *Cryst. Growth Des.*, 2021, **21**, 3469–3476.
24 Y. Xia and G. M. Whitesides, *Angew. Chem., Int. Ed.*, 1998, **37**, 550–575.
25 T. Garting and A. Stradner, *Colloids Surf., B*, 2019, **181**, 516–523.
26 M. Linkert, C. T. Rueden, C. Allan, J.-M. Burel, W. Moore, A. Patterson, B. Loranger, J. Moore, C. Neves, D. Macdonald, A. Tarkowska, C. Sticco, E. Hill, M. Rossner, K. W. Eliceiri and J. R. Swedlow, *J. Cell Biol.*, 2010, **189**, 777–782.
27 M. K. Cheezum, W. F. Walker and W. H. Guilford, *Biophys. J.*, 2001, **81**, 2378–2388.
28 J. C. Crocker and D. G. Grier, *J. Colloid Interface Sci.*, 1996, **179**, 298–310.
29 C. L. Vestergaard, P. C. Blainey and H. Flyvbjerg, *Phys. Rev. E: Stat., Nonlinear, Soft Matter Phys.*, 2014, **89**, 022726.
30 M. Krzywinski and N. Altman, *Nat. Methods*, 2013, **10**, 1041–1042.
31 T. Atherton and D. Kerbyson, *Image Vis. Comput.*, 1999, **17**, 795–803.
32 F. Gomez, R. Dutra, L. Pires, G. R. D. S. Araujo, B. Pontes, P. M. Neto, H. Nussenzveig and N. Viana, *Phys. Rev. Appl.*, 2021, **15**, 064012.
33 J. E. Garrod and T. M. Herrington, *J. Phys. Chem.*, 1970, **74**, 363–370.
34 A. F. Fucaloro, Y. Pu, K. Cha, A. Williams and K. Conrad, *J. Solution Chem.*, 2007, **36**, 61–80.
35 M. Roullet, P. S. Clegg and W. J. Frith, *J. Rheol.*, 2019, **63**, 179–190.
36 S. Ikeda and K. Nishinari, *Biomacromolecules*, 2000, **1**, 757–763.
37 A. S. Parmar and M. Muschol, *Biophys. J.*, 2009, **97**, 590–598.
38 S. Sugiura, M. Nakajima, S. Iwamoto and M. Seki, *Langmuir*, 2001, **17**, 5562–5566.
39 E. Crestel, L. Derzsi, H. Bartolomei, J. Bibette and N. Bremond, *Phys. Rev. Fluids*, 2019, **4**, 073602.
40 C. Loussert, A. Bouchaudy and J.-B. Salmon, *Phys. Rev. Fluids*, 2016, **1**, 084201.
41 J. F. Swindells, C. F. Snyder and R. C. Hardy, *Viscosities of Sucrose Solutions at Various Temperatures: Tables of Recalculated Values*, National Bureau of Standards – United States Department Of Commerce, 1958, vol. 8.
42 H. Brenner, *Chem. Eng. Sci.*, 1961, **16**, 242–251.
43 J. Meunier, *J. Phys., Lett.*, 1985, **46**, 1005–1014.
44 L. Champougny, B. Scheid, F. Restagno, J. Vermant and E. Rio, *Soft Matter*, 2015, **11**, 2758–2770.
45 S. H. Lee, R. S. Chadwick and L. G. Leal, *J. Fluid Mech.*, 1979, **93**, 705.
46 J. Happel and H. Brenner, *Low Reynolds Number Hydrodynamics*, Springer, Netherlands, Dordrecht, 1981, vol. 1.
47 J. C. Crocker, M. T. Valentine, E. R. Weeks, T. Gisler, P. D. Kaplan, A. G. Yodh and D. A. Weitz, *Phys. Rev. Lett.*, 2000, **85**, 888–891.
48 J. C. Crocker and B. D. Hoffman, *Methods in Cell Biology*, Elsevier, 2007, vol. 83, pp. 141–178.
49 J. Leng and J.-B. Salmon, *Lab Chip*, 2009, **9**, 24–34.
50 M. Quintas, T. Brandao, C. Silva and R. Cunha, *J. Food Eng.*, 2006, **77**, 844–852.
51 *Thermodynamic Data for Biochemistry and Biotechnology*, ed. H.-J. Hinz, Springer Berlin Heidelberg, Berlin, Heidelberg, 1986.
52 D. Yang, J. J. Correia, W. F. Stafford III, C. J. Roberts, S. Singh, D. Hayes, R. Kroe-Barrett, A. Nixon and T. M. Laue, *Protein Sci.*, 2018, **27**, 1334–1348.
53 S. Yadav, S. J. Shire and D. S. Kalonia, *Pharm. Res.*, 2011, **28**, 1973–1983.
54 K. Monkos, *Biochim. Biophys. Acta*, 1997, **1339**, 304–310.
55 D. Yang, M. Daviran, K. M. Schultz and L. M. Walker, *Pharm. Res.*, 2021, **38**, 1765–1775.
56 G. Foffi, G. Savin, S. Bucciarelli, N. Dorsaz, G. M. Thurston, A. Stradner and P. Schurtenberger, *Proc. Natl. Acad. Sci. U. S. A.*, 2014, **111**, 16748–16753.

 